Microfocus Small-Angle X-ray Scattering Investigation of the Skin–Core Microstructure of Lyocell Cellulose Fibers

C. E. MOSS,[1] M. F. BUTLER,[1] M. MÜLLER,[2] R. E. CAMERON[1]

[1] University of Cambridge, Department of Materials Science and Metallurgy, New Museums Site, Pembroke Street, Cambridge, CB2 3QZ, United Kingdom

[2] European Synchrotron Radiation Facility, B.P. 220, F-38043 Grenoble Cedex 9, France

Received 31 October 2000; accepted 12 June 2001

ABSTRACT: Skin–core microstructures in hydrated lyocell cellulose fibers were investigated using microfocus small-angle X-ray scattering (SAXS). Both single fibers and fiber cross sections were observed. In all the fibers studied, a thin skin layer was observed in which the voids were smaller in cross section and better oriented than those in the core. The division between skin and core may not be sharp. A draw ratio of 0.80 gave fibers with voids that were shorter, larger in cross section, and more misoriented than the fibers produced with a draw ratio of 1.68. In contrast, there was little difference in void structure between samples coagulated in water and in 25% amine oxide aqueous solution. The results are explained in the context of the spinodal decomposition, which is thought to occur during coagulation. © 2002 John Wiley & Sons, Inc. J Appl Polym Sci 83: 2799–2816, 2002; DOI 10.1002/app.10256

Key words: X-ray microfocus; lyocell; spinodal decomposition; skin–core microstructure; small-angle X-ray scattering

INTRODUCTION

Lyocell fibers, including the commercial fiber Tencel, which are created using a direct dissolution technique,[1] are known to possess a fibril/void microstructure.[2,3] This is thought to result from spinodal decomposition as the cellulose is quenched in a nonsolvent, usually water.[1]

Theoretically, spinodal decomposition could give rise to radial differences in length scale. The depth of quench may vary as a function of distance from the filament surface, as a result of a temperature or solvent gradient, with the skin experiencing a deeper quench than the core.[4,5] This would result in shorter wavelength fluctuations in density in the skin than in the core. Furthermore, the time taken to solidify will increase with increasing distance from the fiber surface,[6] which may also affect the resultant microstructure. Such local differences in microstructure could cause local differences in the ability to swell in water, resulting in internal stresses in the wet fiber and affecting properties in the wet state.[7] There could also be radially varying different susceptibility to dye absorption.[6]

Skin–core microstructures have been observed in experimental lyocell fibers using TEM.[8] A dense cellulosic network, containing small, finely distributed voids with dimensions ranging from 10 to 100 nm was observed. The structure was uniform throughout the cross section, except for a small, highly dense boundary layer.

Correspondence to: R. E. Cameron (rec11@cam.ac.uk).
Contract grant sponsor: Courtaulds Corporate Technology.
Contract grant sponsor: EPSRC.

Journal of Applied Polymer Science, Vol. 83, 2799–2816 (2002)

The aim of the experiments presented here is to explore lyocell microstructure as a function of radial position, using microfocus small-angle X-ray scattering (SAXS). This technique does not require tedious sample preparation and is nondestructive.[9] The effects of varying the processing conditions on overall microstructure and on any possible skin–core structures are also investigated.

EXPERIMENTAL

Preparation of Fiber Samples

Tencel, the lyocell fiber manufactured commercially by Courtaulds, was not used for this experiment because of its relatively small diameter, about 12 μm in the dry state. Instead, a range of lyocell fibers with larger diameters were prepared by Courtaulds by the direct dissolution method used for Tencel, in which wood pulp is dissolved in an amine oxide solvent.[1] All the fibers were spun through a single jet of diameter 200 μm and collected at a constant take-up velocity of 8 mm/min. However, the coagulation bath conditions and the jet velocity used varied between the fibers.

Varying the jet velocity, while keeping the take-up velocity constant, is equivalent to varying the draw ratio, because the draw ratio D_R is the take-up velocity divided by the jet velocity. Two coagulation bath conditions were used: first, water at 5°C and second, 25% amine oxide solution in water at 22°C. These conditions were chosen in an attempt to give different quench depths in the coagulation bath resulting from their different temperatures and chemical compositions. Solvents at 5°C give a deeper quench than at 20°C, and hence should give rise to a finer microstructure as a result of the stabilization of shorter wavelength fluctuations. Furthermore, the deeper the quench, the greater the differentiation in composition between the two phases (cellulose and water in this case), that is, the purer the regions.[10] The depth of quench also depends on the "power" or effectiveness of the non-solvent.[10] For cellulose, pure water is a more effective non-solvent than 25% amine oxide aqueous solution, in that cellulose is soluble in amine oxide.[11] Therefore, water should give a deeper quench than the 25% amine oxide solution. Combining this composition effect with the lower temperature of the water coagulation bath, the water at 5°C should give rise to a significantly deeper quench than the 25% amine oxide aqueous solution at 22°C. Two different draw ratios were also used, 1.68 and 0.80. The draw ratio affects the orientation of the structures within the resultant fiber, with higher draw ratios giving rise to more oriented structures.[6,11,12]

Table I Summary of the Processing Parameters of Each of the Fibers

Solvent D_R	H_2O (5°C)	25% Amine Oxide Solution (aq) (22°C)
1.68	Fiber 1	Fiber 2
0.80	Fiber 3	Fiber 4

The samples are summarized in Table I. It is apparent that by comparing the results of fibers 1 and 2, and of fibers 3 and 4, the effects of coagulation bath conditions on microstructure can be investigated, given that all other processing conditions are constant. Similarly, by comparing the results of fibers 1 and 3, and of fibers 2 and 4, the effects of draw ratio on fiber microstructure can be investigated.

Fiber sections, cut perpendicular to the fiber axis, were prepared as follows. A bundle of fibers about 5 cm in length were wrapped around a hook. The fibers were then covered in hot paraffin wax at about 60–70°C. The wax was allowed to cool, and the wax-encased fibers were microtomed perpendicularly to the fiber axis to give sections. The sections were then mounted on a carbon film–covered copper grid (200-μm mesh), using a glycerol/albumin-based water-soluble adhesive. The paraffin wax was melted off using a Bunsen burner, and residual traces were removed by washing with industrial methylated spirit. The use of a water-soluble adhesive was necessary to allow the fiber sections to swell freely in the water-swollen state, while giving sufficient adhesion to hold the sections in place on the grid.

Both single fibers and fiber sections were tested in the water-swollen state. The fibers were preswollen in water for about 30 min before testing. A water-swollen single fiber was then glued across a washer (diameter $\sim$ 4 mm), which was attached to a goniometer pin. A 0.04-mm-thick layer of mica was fixed in front of the fiber, and a small water-swollen tissue reservoir placed at the base of the washer (see Fig. 1), to encourage capillary flow between the fiber and the mica. This ensured that the water-swollen fibers remained fully hydrated for about 10 min, sufficient time to perform a scan across the fiber. The mounted single fibers and water-swollen sections on copper

grids were aligned using a goniometer, to ensure that the fiber length was perpendicular to the beam. The goniometer head and mounted sample were then placed in the beam on a high-precision translation stage.

Experimental Procedure

The SAXS microfocus experiments were performed at the European Synchrotron Radiation Facility (ESRF) on beamline ID13.[13] Two trips were made to ID13, and the beam size differed between these trips. The data shown in this study were, for the most part, collected on a single trip, for which the beam size was 4 μm. The beam-defining elements in this case were a glass capillary and a 20-μm platinum iridium aperture placed about 10 mm from the capillary. However, some of the data shown were collected on a second trip, for which the beam size was 10 μm. In this case, the beam was defined by 10- and 30-μm apertures. For both trips the camera length was about 1 m, and the beam path between sample and detector was evacuated. These conditions gave a minimum value of the scattering angle s of about 0.008 $Å^{-1}$ for the 4-μm beam and about 0.005 $Å^{-1}$ for the 10-μm beam. With this camera length it was not possible to test the fibers in the dry state because the s range observed was in the wrong regime. Although the s_{min} value of the 10-μm data was lower than that of the 4-μm data (thus giving more scatter in the desired low-angle regime), the larger beam gave a loss of resolution in the scanning direction (denoted z). Where possible, analysis was performed on both the 4- and the 10-μm data.

The beam was scanned across the samples in 4-μm (or 10-μm) steps, depending on the beam size (see Fig. 2). For the sections, the long-distance microscope was used to locate the fiber sections on the grid. A specific point on the sample could then be transferred from the optical center to the beam center because this distance had been previously calculated. Each frame of the scan was 8 s long, which gave the maximum intensity possible before visible beam damage occurred. Two-dimensional SAXS images were collected using a cooled MARCCD camera (4-μm beam experiments) and a Photonic Science image-intensified CCD camera (10-μm beam experiments). Figure 2 shows that on passing from the center to the edge of the single fiber, the proportions of skin and core comprising the thickness will vary. If the skin is relatively thick, the edge frames may be comprised solely of skin.

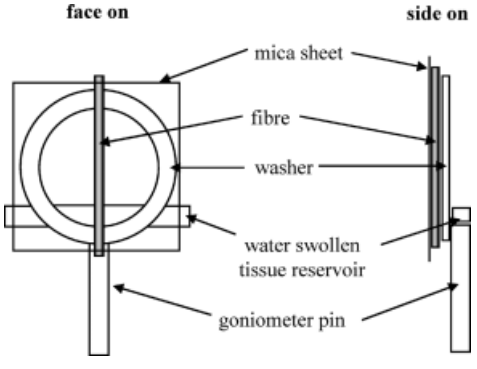

Figure 1 Schematic diagram illustrating the mounting of single fibers.

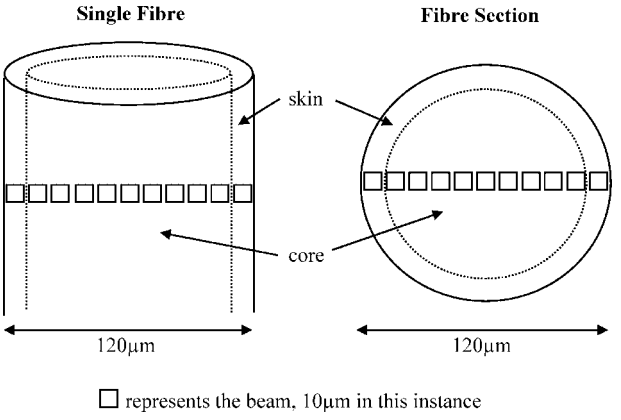

Figure 2 Schematic of a scan across a single fiber and a fiber section.

The diameters of the water-swollen fibers were measured before starting the scan, using the long-distance microscope on ID13. On completing the scan, the fiber diameter was remeasured to check that the fiber was still fully hydrated. At least two scans were made across each fiber type to give an idea of the reproducibility of the results.

Preliminary Data Correction

Prior to data analysis, various corrections were applied to the SAXS images. Background scatter was corrected for by subtracting an average 8-s "blank" image from the sample scatter. A different blank was used for each fiber and was comprised of the extreme edge frames of each scan, where no sample was present. The intensity of the primary beam was assumed to be constant over the short scan times used. The SAXS images were s-mapped, using silver behenate.[14] These procedures were carried out using the software package FIT2D.[15]

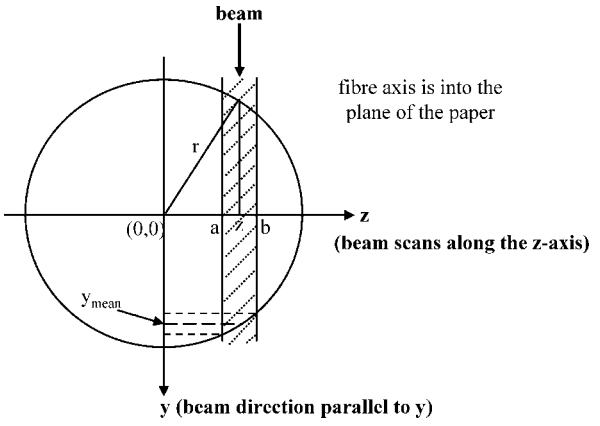

Figure 3 Schematic of the variation in thickness as a function of position across the fiber.

Finally, the single fiber data were normalized to correct for intensity differences between the frames of the scan because of the changing sample thickness across a fiber (see Fig. 3). This correction was not necessary for the fiber sections, which were assumed to be of constant thickness. The scattered intensity depends on the sample thickness and absorbance:

$$I = I_0 t e^{-\mu t} \tag{1}$$

where I is the scattered intensity, I_0 is the primary beam intensity, t is the sample thickness, and μ is the absorbance coefficient of the material.[16] Therefore, to correct for variations in scattered intensity resulting from changing fiber thickness, the scattered intensity is divided by $te^{-\mu t}$. The value of μ for cellulose was calculated from the mass-absorption coefficients of the component elements and the mean density and taken to be 12.4 cm^{-1}. The presence of water in the fibers was ignored, given that the water volume fraction as a function of z-position across the fiber is unknown. However, the calculated absorbance of water of 10.3 cm^{-1} is similar to that of cellulose and so ignoring the water will have little effect on the overall normalization of the scattered intensity.

To normalize using eq. (1), the fiber thickness t must also be calculated for each position on the scan. The fibers have a circular cross section. Hence, the thickness of the fiber at any position along the diameter is defined by a given chord length (see Fig. 3). The beam direction is defined as y, whereas z is perpendicular to the fiber axis x. The equation of a circle in the y–z plane, of radius r and centered on the origin, represents the fiber cross section and is given by

$$y = \sqrt{r^2 - z^2} \tag{2}$$

The beam has a finite thickness and extends between $z = a$ and $z = b$. The mean thickness of the fiber crossed by the beam at this position is given by[17]

$$2y_{\text{mean}} = t_{\text{mean}} = \frac{2}{b-a}\int_a^b y\,dz = \frac{2}{b-a}\int_a^b \sqrt{r^2 - z^2}\,dz \tag{3}$$

The integral in eq. (3) is analytic[17]

$$\int \sqrt{r^2 - z^2}\,dz = \frac{r^2}{2}\sin^{-1}\left(\frac{z}{r}\right) + \frac{z}{2}\sqrt{r^2 - z^2} + c \tag{4}$$

Each frame of the scan was normalized to account for the variations in sample thickness on scanning across the fiber, using eq. (1), on substitution of the appropriate t_{mean} value.

Data Analysis

Ruland analysis[18,19] was used on the SAXS fiber data to calculate the width of the orientation distribution of the voids (B_ϕ) and the average void length projected onto the fiber axis (L_3). The right-hand lobe of the scatter was used in each case, in that this showed better subtraction around the beam stop than the left-hand lobe. For fibers 1, 2, and 4, the s range 9.76×10^{-3} to 0.0184 $Å^{-1}$ was used for each SAXS image, which was divided equally into six azimuths. For fiber 3, the same low s value was used, although the upper limit was taken as 0.0170 $Å^{-1}$ because of the greater amount of noise of the high scattering angle data, and the range divided equally into five azimuths. The resulting azimuths were then fitted using a Lorentzian distribution, and the full width at half maximum (B_{fwhm}) was used to calculate the integral width of the angular intensity distribution (B_{obs}), using[20]

$$B_{\text{obs}} \cong \frac{B_{\text{fwhm}}}{0.63662} \tag{5}$$

Because[19]

$$(sB_{obs})^2 = \left(\frac{1}{L_3}\right)^2 + (sB_\phi)^2 \quad (6)$$

plots of $(sB_{obs})^2$ against s^2, yielded B_ϕ and L_3.

L_3, the projection of the void length onto the fiber axis, was combined with B_ϕ to obtain L, the average length of the voids using

$$L = L_3 \frac{\int_0^{\phi_{max}} \left(\frac{\sec\phi}{B_\phi^2 + 4\phi^2}\right) d\phi}{\int_0^{\phi_{max}} \left(\frac{1}{B_\phi^2 + 4\phi^2}\right) d\phi} \quad (7)$$

where ϕ_{max} is the maximum angle at which voids may be aligned to the axis. It was obtained in a mathematically direct analogy of Ruland analysis,[18,19] by taking the intercept of a plot of ϕ_{obs}^2 against $(1/s^2)$, where ϕ_{obs} is the angle at which each azimuthal curve reaches a background intensity. Equation (7) was evaluated using the MATHEMATICA software package (Wolfram Research, Inc., Champaign, IL).

The SAXS fiber data were also meridionally averaged to obtain the integrated equatorial intensity $\tilde{I}(s)$, equivalent to slit-smeared scatter. The invariant, or scattering power Q, defined as the area under the $s\tilde{I}(s)$ against s curve between 0 and ∞,[21] was approximated by the area under the $s\tilde{I}(s)$ against s plot over the experimental range.

The Bragg equation was used on the peak position of the $s\tilde{I}(s)$ against s plots to give a value of pseudolateral order. Strictly, the lateral order should be calculated from the peak position of the $\tilde{I}(s)$ against s plots, which will occur at lower angles (corresponding to larger spacings). However, the relatively high s_{min} values meant that the interference peak was partially or fully obscured by the beam stop. The peak position of the $s\tilde{I}(s)$ against s plots will not give absolute lateral order values, but any trends should be valid.

RESULTS

Microfocus SAXS of Scans Across Single Fibers

Fiber Thickness

The diameters of the water-swollen fibers, measured using the long-distance microscope on ID13, are recorded in Table II. Fibers 1 and 2, prepared using the higher draw ratio of 1.68, have smaller diameters in the dry state than those of fibers 3 and 4, prepared using the lower draw ratio of 0.80. This is to be expected, given that the higher the draw ratio, the greater the load on the filament as it passes through the air gap, and thus the thinner the diameter of the resultant fiber. The more highly drawn samples also swelled less on hydration.

Table II Comparison of the Diameters of Fibers in Both Dry and Water-Swollen States

Fiber Type	Dry Diameter (μm)	Wet Diameter (μm)	Percentage Increase on Swelling
1	50	70	40
2	50	65	30
3	80	120	50
4	80	120	50
Tencel	12	18	50

Values for the commercial fiber Tencel are included.

SAXS Area Plots

Figure 4 shows the SAXS area patterns of a center and edge frame for fibers 1, 2, 3, and 4, which were background subtracted and volume normalized as described. The center and edge frames of the fibers all show scatter elongated along the equator, which implies that the voids are anisotropic, long and narrow, and have a preferred orientation along the fiber axis. Therefore the processing conditions used to prepare the fibers give rise to the expected anisotropic void system of lyocell fibers. For each fiber, the scatter of the center frame is more intense than that of the edge frame, even after correction for thickness effects. The shape of the scatter also appears to vary slightly between the center and edge frames. The extent of the meridional broadening appears to be larger in each case for the center frame than for the edge frame.

Azimuthal Analysis

The trends in B_ϕ, L_3, and L with z-position, obtained from Ruland analysis, are shown in Figures 5, 6, and 7, respectively. For each frame, the $z = 0$ position is taken as the position of the center of the fiber. In each case the results of the two scans are shown to give a measure of the repeat-

Fibre	Centre	Edge
1	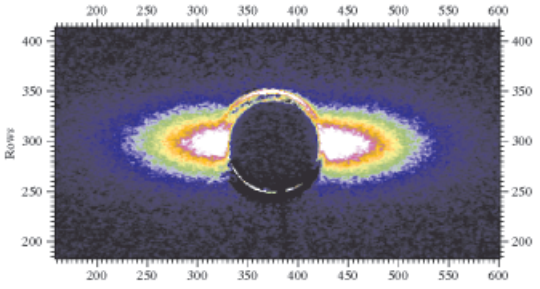	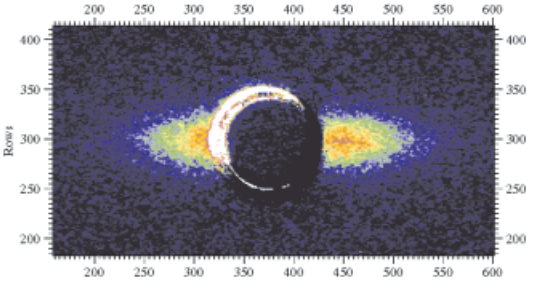
2	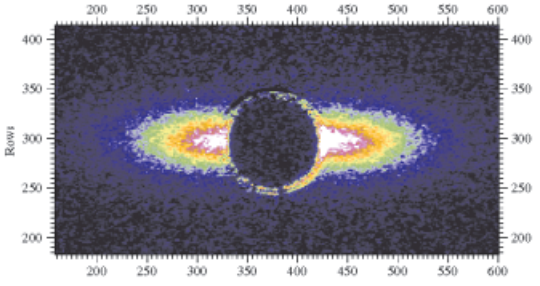	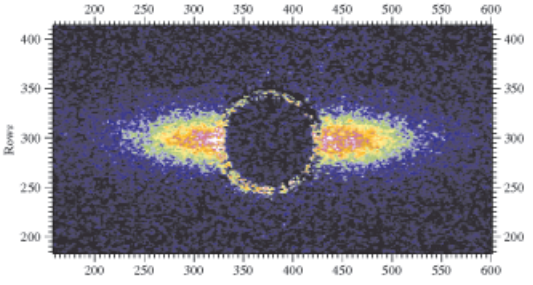
3	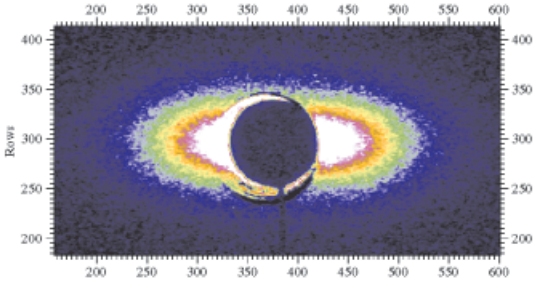	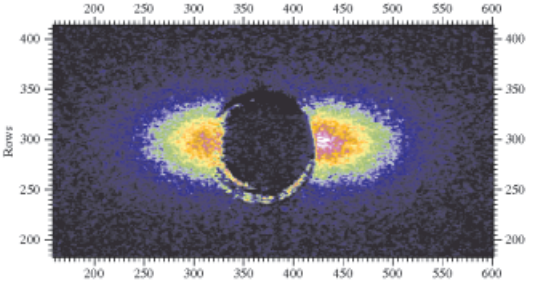
4	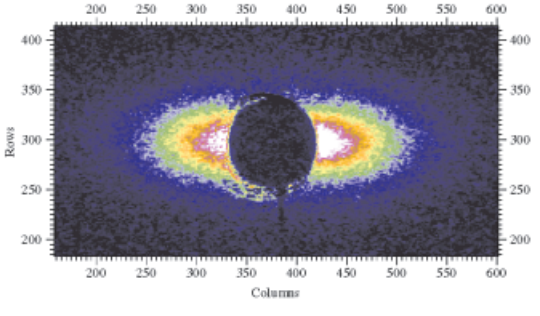	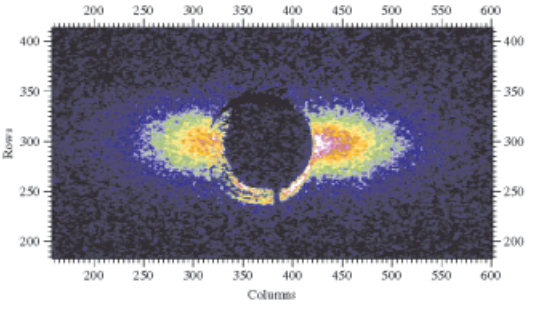

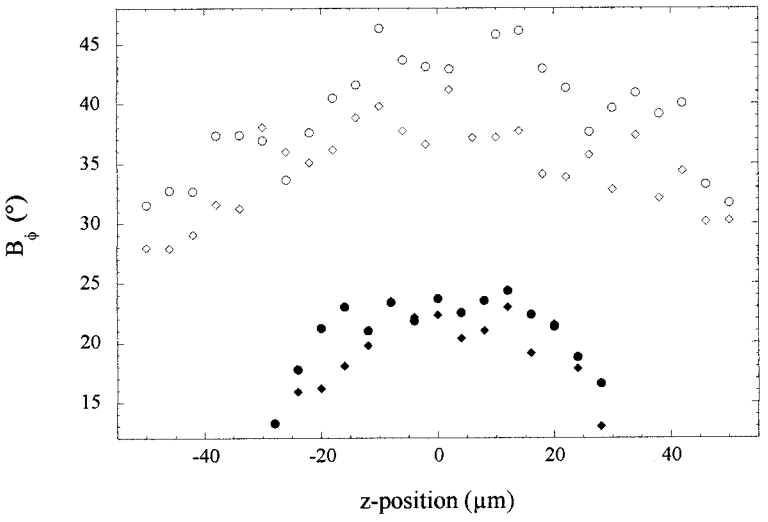

Figure 5 Trends in the width of the orientation distribution of the voids B_ϕ as a function of z-position across fiber 1 (●), fiber 2 (◆), fiber 3 (○), and fiber 4 (◇). The center of each fiber is at $z = 0$. The beam size was 4 μm.

ability. From Figure 5 it is obvious that, for each fiber, B_ϕ varies as a function of z-position, with the edges of the fiber having a smaller B_ϕ than that of the center, that is, the voids in the edge are more highly oriented than those of the center with the fiber axis. This is evidence of some form of skin–core effect.

Table III gives B_ϕ values for the edge and center of each of the fibers. It is clear that varying the coagulation bath conditions does not significantly affect the orientation distribution of the voids; in contrast, varying the draw ratio does affect the orientation distribution of the voids. In both cases the fiber prepared using the higher draw ratio 1.68 (fibers 1 and 3) has a more highly oriented void system than the fiber prepared using the lower draw ratio 0.80 (fibers 2 and 4). Furthermore, the more highly oriented fibers (1 and 2) appear to show a greater differential in B_ϕ between the skin and core than for the less well oriented fibers (3 and 4).

Figures 6 and 7 show the values of L_3 (the projected void length onto the fiber axis) and L (the actual void length) across the fibers. It is clear that any trends in z are similar for L_3 and L, indicating that changes in L_3 are not simply a consequence of changes in the orientation distribution, changing the projected length onto the fiber axis. For fibers 1, 2, and 3 there appears to be no trend in L_3 and L with z-position across the fiber. In the case of fiber 4 there may be a slight trend in L as a function of z-position. Although this increase is small from center to edge ($\sim$ 15 Å for L), the fact that it occurs at both edges and for both repeat results suggests that it is real.

Tables IV and V give the average L_3 and L values. The draw ratio appears to affect the average void length. The fibers prepared using the higher draw ratio 1.68 (fibers 1 and 2) have a larger average void length than that of the fibers processed using the lower draw ratio 0.80 (fibers 3 and 4). In contrast, varying the coagulation bath conditions does not appear to affect the average void length of the resultant fiber.

The Invariant

Figure 8 shows the trends in Q with z-position for the fibers. In each case both the 10-μm and the 4-μm data sets are shown, represented by circles when presenting the azimuthal results. It is clear that for each fiber, Q varies with

Figure 4 Comparison of the microfocus SAXS center and edge frames of fibers 1–4. The images were normalized to take into account variation in thickness across the fiber. The arbitrary intensity scale is 0–80 for fibers 1 and 2 and 0–50 for fibers 3 and 4, where blue is the lower limit and white the upper limit.

Table III Values of Width of Orientation Distribution of Voids (B_ϕ), Calculated from the Scattering Profile of a Beam Passing Through the Center and Edge of the Fiber, for Each Processing Condition

Solvent D_R	H_2O (5°C)	25% Amine Oxide Solution (aq) (22°C)
1.68	Center: 21.7 ± 1.7°	Center: 20.5 ± 1.3°
	Edge ≈ 14°	Edge ≈ 12°
	Decrease ≈ 35%	Decrease ≈ 41%
0.80	Center: 40.9 ± 2.9°	Center: 37.0 ± 1.9°
	Edge ≈ 32°	Edge ≈ 29°
	Decrease ≈ 22%	Decrease ≈ 22%

The quoted center values are the means ± SD of the center frames, over which there is no significant trend for the two separate data sets. The edge values are the approximate average of the edge frames of the two data sets.

z-position, with Q being larger at the center than at the edge of the fiber. Because the data were corrected for variations in sample thickness and because the electron density difference between the two phases (cellulose and water-filled void) is the same in each case, Q is directly proportional to the volume fraction product (vfp) of the two phases:

$$Q \propto v(1 - v) \tag{8}$$

where v is the volume fraction of cellulose and $(1 - v)$ is the volume fraction of water-filled voids, although this may not be exactly obeyed because the values of Q are calculated using the available experimental angular range and are thus only approximations. The highest possible value of vfp is 0.25, given when the volume fractions of both phases is 0.5. As vfp decreases from 0.25, the ratio of the volume fractions becomes more unequal, in which case the volume fraction of one phase decreases while the volume fraction of the other phase increases (see Fig. 9). Therefore, the decrease in vfp from center to edge suggests a decrease in the amount of one phase and a corresponding increase in the second phase. Without further information it is not possible to say which phase shows the increase in volume fraction, and which shows the decrease.

For each fiber, the trends in Q with z-position are very similar. However, it is not possible to compare the relative Q values of the different fibers, given that Q depends on the intensity of the primary beam, and the data have not been normalized for variations in primary beam intensity.

Lateral Order

Figure 10 shows the trends in pseudolateral order with z-position for the fibers, for data obtained using the 10-μm beam size. It was not possible to obtain reliable peak positions for the 4-μm data because of the noise of the data. It is obvious that for each fiber, pseudolateral order varies as a function of z-position, the center of the fiber hav-

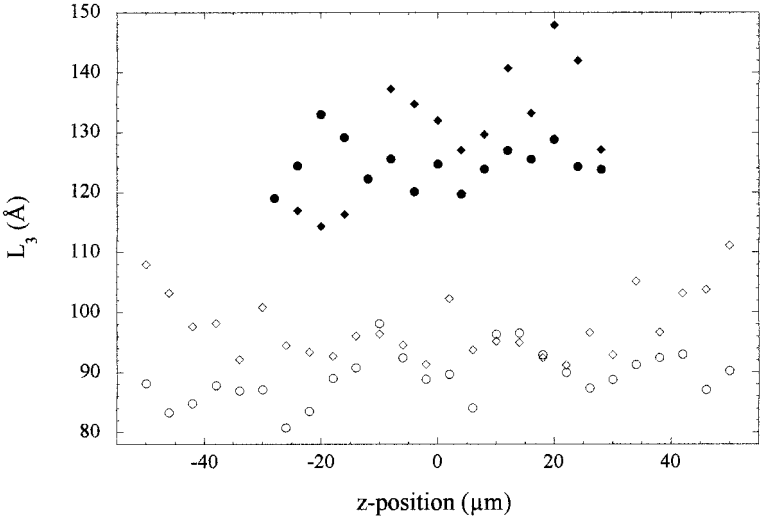

Figure 6 Trends in the average void length, projected onto the fiber axis L_3, as a function of z-position across fiber 1 (●), fiber 2 (◆), fiber 3 (○), and fiber 4 (◇). The center of each fiber is at $z = 0$. The beam size was 4 μm.

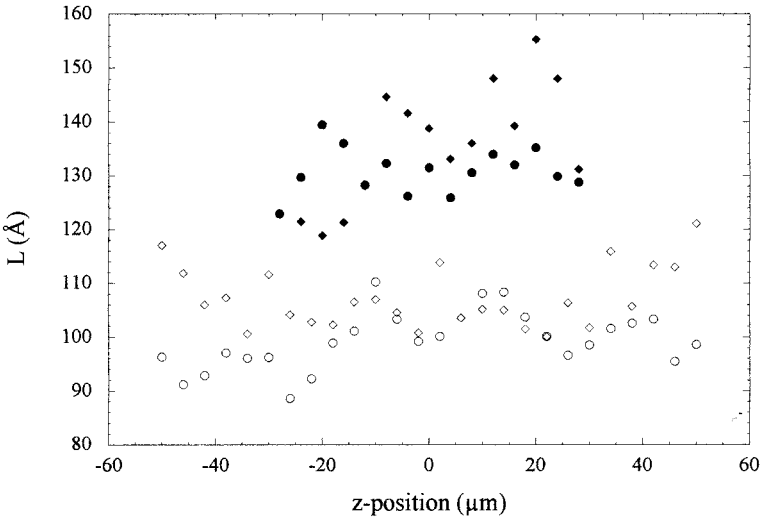

Figure 7 Trends in the average void length L as a function of z-position across fiber 1 (●), fiber 2 (◆), fiber 3 (○), and fiber 4 (◇). The center of each fiber is at $z = 0$. The beam size was 4 μm.

ing larger pseudolateral order values than those of the edges. This is evidence of some form of skin–core effect, with respect to distribution and cross-sectional dimensions of the two phases.

Varying the processing conditions also affected the pseudolateral order of the resultant fibers (see Table VI). Changing the coagulation bath conditions does not significantly affect the pseudolateral order of the resultant fiber, whereas changing the draw ratio does affect the pseudolateral order of the resultant fiber. In both cases the fiber processed using the higher draw ratio 1.68 (fibers 1 and 2) have a smaller pseudolateral order than those produced using the lower draw ratio 0.80 (fibers 3 and 4).

Relative Thickness of the Skin and Core

This section presents preliminary investigations of the relative thickness of the skin and core of the fibers. The trends in Q obtained for the 4-μm beam size are compared with theoretical profiles calculated for a number of fixed skin thicknesses, assuming a sharp transition from skin to core.

The beam passes through the sample in the y direction. At a given position z in the scan, the fraction of core cut by the beam is $f(z)$ and the fraction of skin is $[1 - f(z)]$. If the position of the beam z is greater than the core radius r_c and less than the skin thickness r_s, the beam cuts entirely through skin, and $f(z) = 0$. If z is less than r_c, then

$$f(z) = \frac{\sqrt{r_c^2 - z^2}}{\sqrt{(r_c + r_s)^2 + z^2}} \tag{9}$$

This is illustrated schematically in Figure 11. When $z = 0$, and the beam passes through the center of the sample, the core fraction simplifies to give

Table IV Average Values of Projected Length of Voids onto the Fiber Axis L_3 for Each Processing Condition

Solvent D_R	H_2O (5°C)	25% Amine Oxide Solution (aq) (22°C)
1.68	119±7Å	129 ± 8 Å
0.80	91±4Å	Center ≈ 93 Å Edge ≈ 110 Å

For fibers 1, 2, and 3 the values given are the means ± SD of two data sets across the entire fiber diameter. For fiber 4 approximate values for a beam passing through the center and the edge are given.

Table V Average Values of Length of Voids (L) for Each Processing Condition

Solvent D_R	H_2O (5°C)	25% Amine Oxide Solution (aq) (22°C)
1.68	131±4Å	136 ± 11 Å
0.80	99±5Å	Center ≈ 100 Å Edge ≈ 115 Å

For fibers 1, 2, and 3 the values given are the means ± SD of two data sets across the entire fiber diameter. For fiber 4 approximate values for a beam passing through the center and the edge are given.

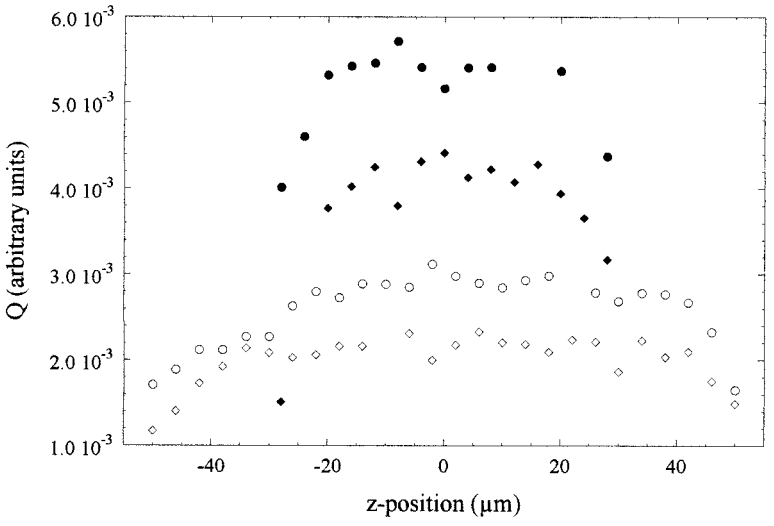

Figure 8 Trends in the invariant (or scattering power) Q as a function of z-position across fiber 1 (●), fiber 2 (◆), fiber 3 (○), and fiber 4 (◇). The center of each fiber is at $z = 0$. The beam size was 4 μm.

$$f(0) = \frac{r_c}{r_c + r_s} \tag{10}$$

For each frame of the scan,

$$Q(z) = Q(\text{core})f(z) + Q(\text{skin})[1 - f(z)] \tag{11}$$

It is assumed that the experimental value of Q of the edge frames is equivalent to Q(skin). This is valid, provided that the edge frame is in fact from the very edge of the fiber, and that the beam size is smaller than that of the skin. In many cases the very edge frame was of too low an intensity for analysis, and the subsequent frame was taken to represent the edge, which may introduce an error. Q(core) may be calculated from eq. (11) at $z = 0$, taking the experimental value of $Q(0)$ as the average Q value over the center frames for which there was no significant trend and assuming a chosen value of $f(0)$.

This allows the calculation of theoretical $Q(z)$ values as a function of z-position, based on the varying proportions of skin and core on scanning across the fiber. This is done for various

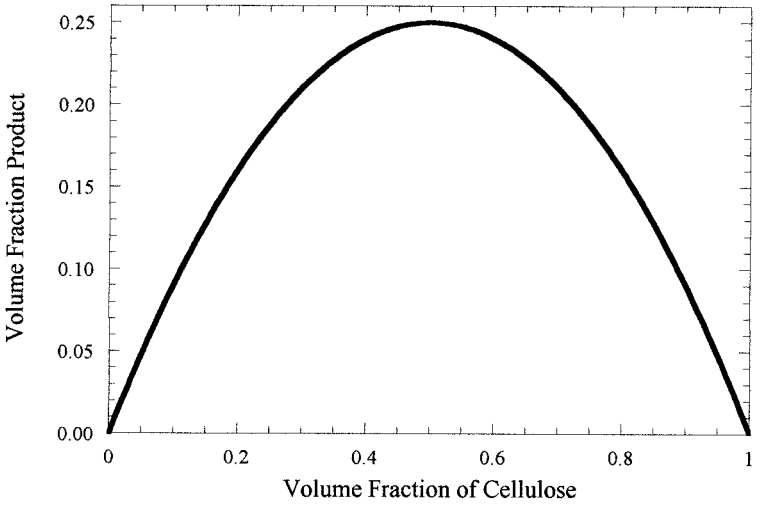

Figure 9 Relationship between individual volume fraction and the volume fraction product.

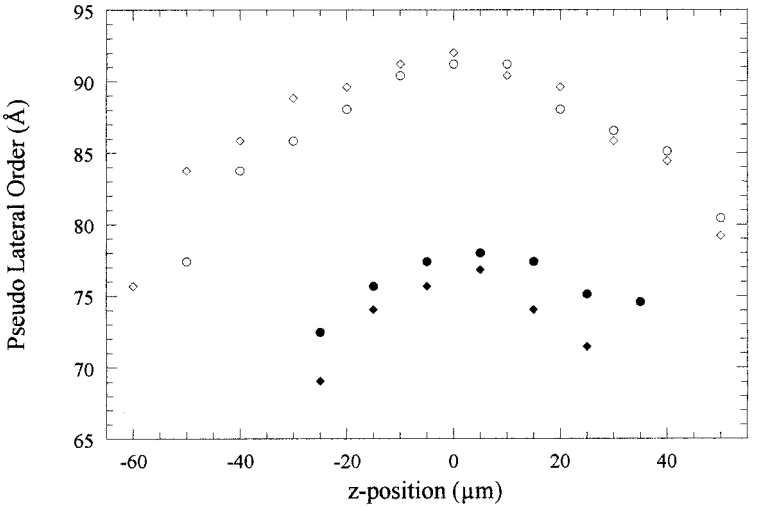

Figure 10 Trends in the pseudolateral order as a function of z-position across fiber 1 (●), fiber 2 (♦), fiber 3 (○), and fiber 4 (◇). The pseudolateral order is calculated by applying the Bragg equation to the peak position of a plot of $s\tilde{I}(s)$ against s. The center of each fiber is at $z = 0$. The beam size was 10 μm.

core radii, by substituting fixed values for r_c and r_s into eq. (9). Hence, f and then Q are calculated as a function of the z-position using eqs. (9) and (11), respectively. For each fiber, core radius values are chosen to give a known core fraction at $z = 0$, to give a series of Q against z-position curves, which are then compared with the experimental data.

Figures 12(a)–12(d) show comparisons of the experimental Q values with the theoretical curves. For each fiber, the trends in the experimental Q values with z-position are very similar. For all four fibers the trends in the experimental data do not correlate with the theoretical curves generated using the extreme $f(0)$ values of 0.3 (thin core) and 0.95 (very thin skin, smaller than the 4-μm beam). For fibers 1 and 2, the theoretical profile generated using $f(0) = 0.8$ appears to give the best fit to the experimental data. For fibers 3 and 4, the theoretical profiles generated by $f(0)$ values of 0.8 and 0.6 most closely model the experimental data. Because of the noise of the data it is impossible to make a more quantitative esti-

Table VI Values of Pseudolateral Order, Calculated from the Scattering Profile of a Beam Passing Through the Center and the Edge of the Fiber, for Each Processing Condition

Solvent D_R	H_2O (5°C)	25% Amine Oxide Solution (aq) (22°C)
1.68	Center: 78 ± 3 Å	Center: 76 ± 0.8 Å
	Edge ≈ 73 Å	Edge ≈ 70 Å
	Decrease ≈ 6%	Decrease ≈ 8%
0.80	Center: 91 ± 0.5 Å	Center: 91 ± 0.8 Å
	Edge ≈ 79 Å	Edge ≈ 78 Å
	Decrease ≈ 13%	Decrease ≈ 14%

Pseudolateral order is calculated by applying the Bragg equation to the peak position of a plot of $sI(s)$ against s. The quoted center values are the means ± SD of the center frames, over which there is no significant trend for the two separate data sets. The edge values are the approximate average of the edge frames of the two data sets.

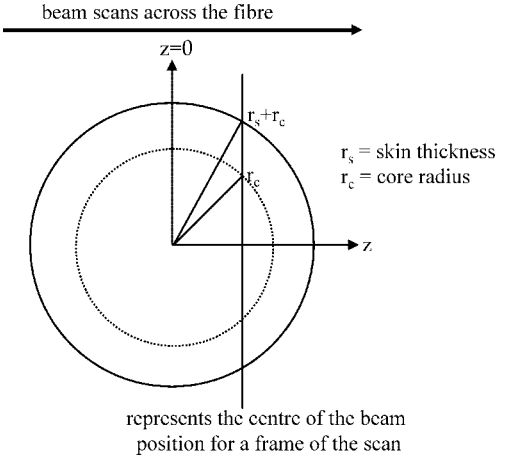

Figure 11 Schematic of the fiber cross section showing the definitions of r_c (radius of core) and r_s (radius of skin).

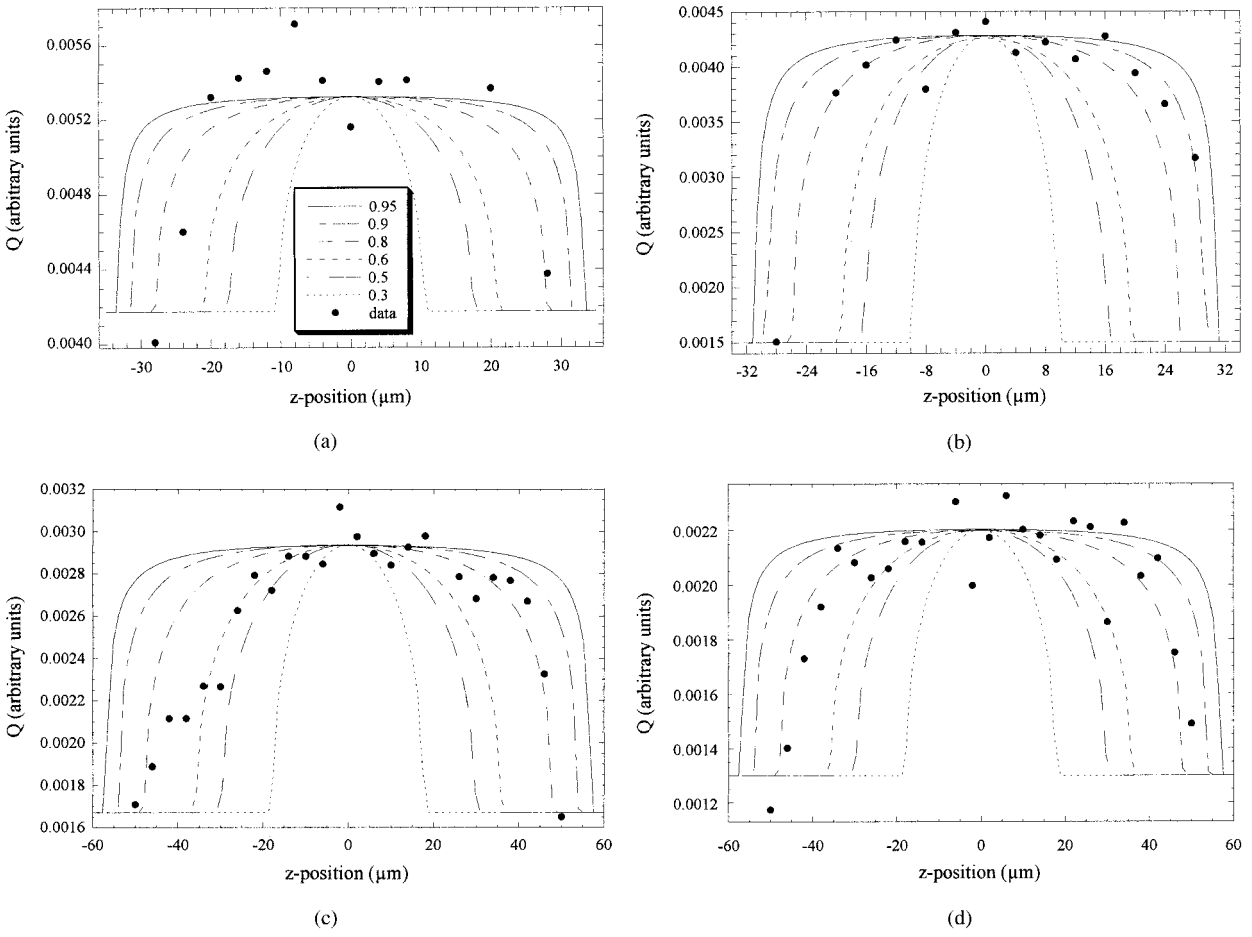

Figure 12 Comparison of theoretical and experimental trends in the invariant Q with z-position for (a) fiber 1, (b) fiber 2, (c) fiber 3, and (d) fiber 4. The theoretical values are calculated, as described in the text, for fibers with the same overall radius, but with differing ratios of skin to core. The chosen core fractions are shown in the legend of (a).

mate. Therefore, within the limits of the data there appears to be no significant difference in core fraction $f(0)$ as a result of the varying processing conditions. An equivalent analysis on the B_ϕ data gave similar values for $f(0)$.

To conclude, for each fiber the experimental trends in B_ϕ and Q are most closely modeled by theoretical profiles generated using a core fraction $f(0)$ of approximately 0.8. This suggests that the fibers are composed of a core that is thicker than skin. For $f(0) = 0.8$, fibers 1 and 2 have a skin thickness of about 7 μm, and fibers 3 and 4 of about 12 μm. This analysis requires the assumption of a sharp transition between skin and core. Because the data only loosely fit the theoretical curves, it would seem likely that the boundaries are somewhat blurred and that there is some degree of continuous variation.

SAXS from Scans Across Fiber Sections

Problems Associated with the Fiber Sections

A number of factors, arising from sample preparation methods and experimental setup, limited the success of scans across the fiber sections. The main sample preparation problem was the slippage of the fiber bundle through the wax while microtoming the sections. Hence, instead of obtaining thin sections of constant thickness, the resulting sections were wedge shaped. This affected the scatter, giving SAXS images that were no longer isotropic. Preparation of the sections from a fiber bundle resulted in the sections overlapping, thus making it extremely difficult to obtain a scan across an entire section diameter. Mounting the sections on a copper grid also resulted in parts of the sections being obscured by

the grid, again making it difficult to scan across an entire section. Further problems arose from the available s range of the data and a significant part of the scatter was not visible. For fibers 1 and 2, there tended to be an insufficient number of scattering frames to constitute a scan across the diameter of a water-swollen fiber section. The probable explanation for this is that the scan was along a chord and not the diameter, which could be the result of problems encountered in translating the optical center of the microscope to the beam center, which would obviously be more significant for the smaller diameter fibers.

It therefore proved difficult to obtain usable SAXS scans across the fiber sections and it is not possible to quantitatively discuss changes in the microstructure, as a function of position across the section diameter, or as a function of the different processing conditions. However, limited SAXS data for fiber sections 1 and 3 were collected. These data were chosen in preference to other data collected, because in these cases the scans were definitely across a single fiber section, and the intensity of the scatter was symmetric across the scan, indicating that these were not wedge-shape samples. In the case of fiber section 1, the number of frames showing scatter is insufficient for the scan to be across the diameter of the section, and it is thus assumed that the scan is along the chord shown in Figure 14. If the skin of fiber 1 is of the order of 7 μm, as calculated above, then the scan across section 1 is mainly through the skin. For fiber 3, the number of frames showing scatter corresponds to the scan being approximately across the diameter of the section.

SAXS from Scans Across Fiber Sections 1 and 3

SAXS from fiber sections 1 and 3, center, edge, and edge subtracted from center frames, are shown in Figure 13. For each fiber section, the center, edge, and center minus edge frames are displayed using the same intensity scale, to allow a direction comparison of the images. However, different scales are used for the two sections. The section 1 images were obtained using the 4-μm beam, and the section 3 images using the 10-μm beam. From the center and edge frames of each section, it is clear that the scatter is approximately isotropic, indicating that the voids are isotropic in the plane perpendicular to the fiber axis.

For both fiber sections, the intensity of the scatter of the center frame is higher than that of the edge frame, as reflected by the residual scatter on subtraction of the edge frame from the center frame. For fiber 3, this difference in scattered intensity between the center and edge frames is far greater than that for fiber 1. This is probably because the scan across section 1 is along a chord, whereas that of section 3 is along the diameter. Therefore, the center frames of fiber 1 may not be an accurate reflection of the core microstructure (see Fig. 14).

For each SAXS image the data were integrated around circles of constant scattering angle to obtain one-dimensional plots of intensity I against scattering angle s. Figures 15(a) and 15(b) show the I against s plots of sections 1 and 3 as a function of z-position. In both cases there appears to be a steady increase in intensity on progressing from the edge to the center frames. It is obvious that there is a difference in the shape of the scattering curves between the edge and center frames of fiber section 3. The curves correlate at low and high s, but deviate from each other in the intermediate region. This suggests that there is a size difference between the void cross sections, of the core and the skin. This difference in shape is not evident for fiber section 1. In this case the edge and center frames appear to correlate well throughout the entire s range. This is probably a consequence of the scan across section 1 being along a chord predominantly through the skin, as discussed earlier, as opposed to being along a diameter for section 3.

On comparing the center and edge frames of sections 1 and 3, there is a difference in shape of the I against s curves between the fiber types. For section 1, strong scatter is seen for the s range of about 0.01–0.02 Å^{-1}, after which the intensity of the scatter tails off with increasing s. However, for section 3 in the s range of about 0.005–0.01 Å^{-1}, only the tail end of the scatter is visible. It is therefore assumed that the main region of scatter is at lower s than the experimental s range. Therefore, section 3 scatters to lower scattering angles than those of section 1 and, thus, the void cross sections are larger in fiber section 3 than those in fiber section 1.

Finally, a comparison is made between the I against s plots of sections 1 and 3 [Figs. 15(a) and 15(b)], and the I against s plots of the thin equatorial slices of *single fibers* 1 and 3 [Fig. 16(a) and 16(b)]. The I against s curves of the fiber cross section and single fiber should be comparable because both represent scattering from the void cross sections alone. At the edge of the fiber, the scattering is likely to be exclusively from the skin

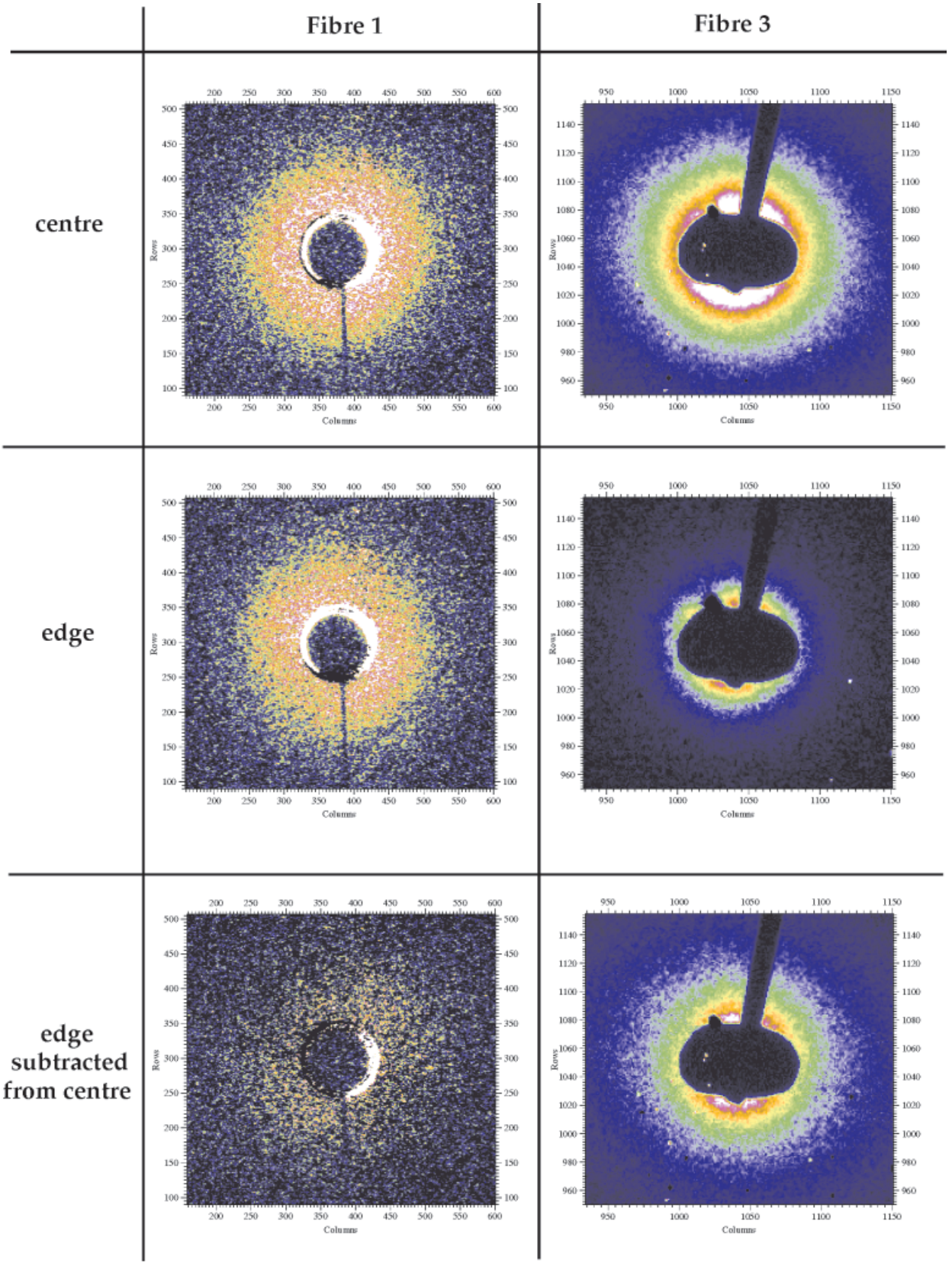
Fibre 1
Fibre 3
centre
edge
edge subtracted from centre
Rows
Columns

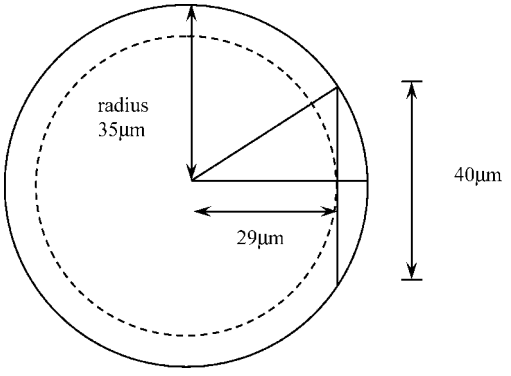

Figure 14 Schematic showing the position of the chord scanned across section 1. The water-swollen diameter of the fiber is 70 μm.

(see Fig. 2) and thus should be very similar to the scatter from the edge of a fiber section. At the center of the fiber, the scatter is a weighted average of that from skin and core. Because the skin appears to be quite thin, the scatter will be weighted toward that of the core and should be similar, though not identical to, scatter from the center of a fiber section.

For fiber 1, the I against s curves of the section [Fig. 15(a)] have roughly the same shape as the edge scattering curves of the single fiber [Fig. 16(a)]. This is to be expected, given that the scan across fiber section 1 is thought to be across a chord composed mainly of skin. For fiber 3, the I against s plots of fiber section [Fig. 15(b)] and the single fiber [Fig. 16(b)] show the same general shape, the center frames scattering to higher intensity than the edge frames in both cases. The ability to compare fiber and fiber section data in this way is a strength of the microfocus technique.

For the edge frames of fiber section 1, the beginning of the shoulder, indicative of lateral order, is visible, giving an approximate lateral order size in the region of 100–200 Å. For the center frames of fiber 1 and all frames of fiber 3 the shoulder is not visible, suggesting that in these cases lateral order is greater than 200 Å. These trends match those of the pseudolateral order shown in Figure 10.

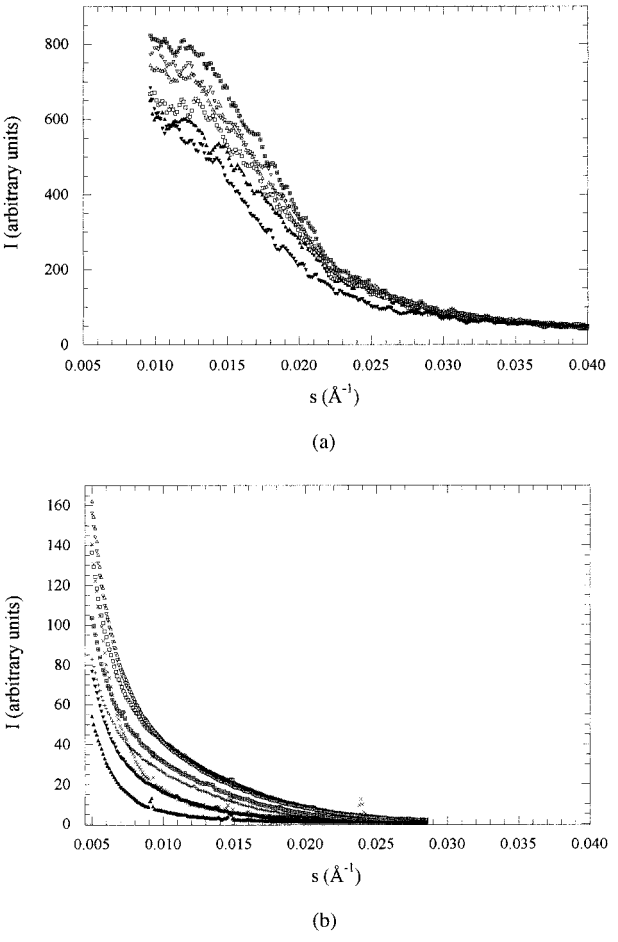

Figure 15 (a) Intensity versus scattering angle for section 1 as a function of z-position: $z = -18$ μm, 18 μm (▲, ▼); $z = -10$ μm, 10 μm (✷, ⊞); $z = -2$ μm, 2 μm (△, ▽). (b) Intensity versus scattering angle for section 3 as a function of z-position: $z = -55$ μm, 55 μm (▲, ▼); $z = -45$ μm, 45 μm (×, +); $z = -25$ μm, 25 μm (✷, ⊞); $z = -5$ μm, 5 μm (△, ▽).

To conclude, fiber section 3 shows differences in scattering between the center and edge frames, which suggests that there is some form of skin–core microstructure. Furthermore, the differences in shape of the I against s curves of fiber sections 1 and 3 suggests that the scattering objects, the void cross sections, of fiber section 3 are larger

Figure 13 Comparison of the microfocus SAXS images of fiber sections 1 and 3. The center and edge frames are shown, together with the center with edge subtracted. It is thought that the scan across section 1 was across a chord rather than a diameter and that the center frame actually passed through material that was primarily skin. The arbitrary intensity scale is 0–800 for fiber section 1 and 1–250 for fiber section 3, where blue represents the lower limit and white the upper limit.

than those of fiber section 1. This is in agreement with the data obtained from the fibers themselves.

DISCUSSION

Trends in Void Microstructure

Figure 17 schematically illustrates the differences in void structure between the skin and core. The voids in the skin are more highly oriented than those of the core, whereas except for fiber 4, the length of the voids along the fiber axis remains constant across the fiber. Lateral order and volume fraction product (vfp) both increase from the skin to the core. Although there is no unique interpretation of these parameters, on the basis of spinodal decomposition theory the trends in lateral order and vfp may be interpreted as an increase in cross-sectional dimensions of the cellulose and voids from the skin to the core. This increase in cross-sectional dimensions is shown pictorially on Figure 17 as an increase in the void diameter from skin to core. Within the limits of the experimental data no significant difference is observed between the skin-to-core ratios of the fibers. However, the different processing conditions used to prepare the fibers do appear to affect the microstructure of the resultant fibers.

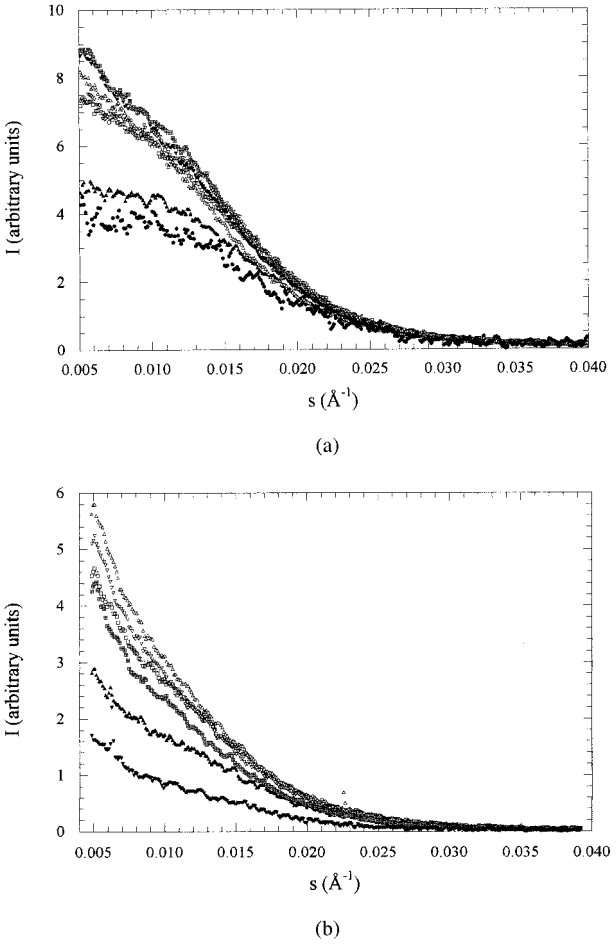

Figure 16 (a) Intensity versus scattering angle for fiber 1 as a function of z-position: $z = 35$ (●); $z = -25$ μm, 25 μm (△, ▼); $z = -15$ μm, 15 μm (✷, ⊞); $z = -5$ μm, 5 μm (△, ▽). (b) Intensity versus scattering angle for fiber 3 as a function of z-position: $z = -50$ μm, 50 μm (▲, ▼); $z = -40$ μm, 40 μm (✷, ⊞); $z = -20$ μm, 20 μm (△, ▽).

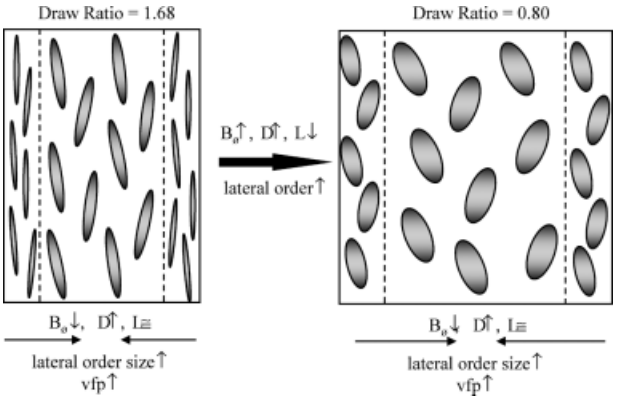

Figure 17 Radial variations in void microstructure of lyocell fibers and the differences in microstructure between (a) high draw ratio (1.68) fiber (fiber 1) and (b) low draw ratio (0.80) fiber (fiber 3). Both fibers were prepared from a water coagulation bath at 5°C. B_ϕ, width of the orientation distribution of the voids; D, average void diameter; L, average void length; vfp, volume fraction product.

The changes in void microstructure as a result of varying the draw ratio are also shown pictorially in Figure 17. The fibers processed using the higher draw ratio 1.68 (fibers 1 and 2) have longer, thinner voids, which are more highly oriented with the fiber axis than those produced using the lower draw ratio 0.80 (fibers 3 and 4).

In contrast, changing the coagulation bath conditions from water at 5°C (fibers 1 and 3) to 25% amine oxide aqueous solution at 22°C (fibers 2 and 4) does not appear to affect the void structure of the resulting fiber. This is surprising, given that water at 5°C is expected to give a deeper quench than that given by 25% amine oxide aqueous solution at 22°C and to result in a finer, purer microstructure. Furthermore, Mortimer and Péguy[11] found that varying the composition of the coagulation bath affected bulk properties. The ex-

tension at break and the extent of fibrillation both decreased with increasing NMMO concentration. Varying the temperature of the coagulation bath also gave clear trends, with tenacity and extension at break both decreasing with increasing spin bath temperature. In view of these changes in bulk properties, it is surprising that no differences in microstructure are observed for the fibers prepared using the different coagulation bath conditions.

Origins of Skin–Core Microstructural Differences

The radially varying microstructure observed for these lyocell cellulose fibers is in marked contrast to the radially constant orientation and lateral organization observed using microfocus SAXS on flax fibers.[22] The scattering patterns observed for flax using microfocus SAXS are similar to those observed here, although the calculated misorientation values are lower (9°). (The patterns do show a narrower streak, consistent with a smaller value, but the value calculated could also be influenced by the fact that these authors used a linear regression of azimuthal width against radial angle rather than Ruland analysis.) Fibers extracted from the native plant therefore appear to be uniform in structure, whereas those regenerated through spinning from solution have imposed radial microstructural variation, even though they possess a similar fibril–void microstructure.

In the fibers studied here, the skin is more highly oriented than the core. This is a common phenomenon of all spinning processes,[6] and may be attributed to the uneven radial distribution of the stress, or the relatively rapid solidification of the outer layer of the filament on entering the coagulation bath compared with the longer solidification time of the core. Fiber 4 also shows an increase in average void length from the core to the skin. Presumably, this is a consequence of the corresponding increase in orientation from core to skin, as a more highly oriented structure favors the formation of long voids.

The length scale of the microstructure is also thought to differ radially as a consequence of spinodal decomposition kinetics. It is expected that the skin will experience a deeper quench than that of the core, which will result in shorter wavelength density fluctuations in the skin than in the core. Furthermore, the skin will solidify more quickly than the core. Hence, in the skin, the spinodal decomposition mechanism will still be in the early stages, giving a fine, interconnected network. The core will take longer to solidify, meaning that the spinodal structure has the opportunity to coarsen. The resulting core morphology will have larger, and maybe fewer, voids than the skin. These considerations suggest that the increase in observed lateral order from skin to core is simply a consequence of the core's having a coarser microstructure than the skin. This hypothesis is supported by the larger void cross-sectional dimensions of the core than those of the skin, as determined from the fiber section data.

Finally, the observed skin–core microstructure correlates well with work by Fink et al.,[8] in which TEM was used to observe the differences in microstructure across fiber cross sections prepared using a range of coagulation bath media. Significantly, and in agreement with the data presented here, using a water coagulation bath, Fink et al. observed a very thin skin layer (thickness not given) consisting of a fine, highly oriented network, compared with a large core region, which was coarser and less well oriented.

Origins of Variations in Microstructure with Changing Draw Ratio

The majority of the trends in microstructure with varying draw ratio are a result of the changing load imposed on the filament as it passes through the air gap. The higher the draw ratio, the greater the load on the filament as it passes through the air gap. The observed increase in orientation with increasing draw ratio is a well-known phenomenon,[6] and is simply a consequence of the higher load being able to orientate the structure more efficiently toward the fiber axis. Presumably, the higher average void length of the high draw ratio fibers is also a consequence of the more highly oriented structure, thus allowing the formation of longer voids. The high draw ratio fibers also have a smaller diameter and a smaller lateral period than those of the low draw ratio fibers. These factors are closely linked and are, again, a result of the higher load placed on the high draw ratio filament during processing.

CONCLUSIONS

The microfocus SAXS experiments showed differences in microstructure between the skin and core of the fibers. Limited studies on the effects of processing parameters on microstructure were also

performed. Changing the draw ratio from 1.68 to 0.80 affected the microstructure of the resultant fiber, the higher draw ratio giving rise to longer, thinner, more highly oriented voids. In contrast, no differences in microstructure were observed on changing the coagulation bath conditions from water at 5°C to 25% amine oxide aqueous solution at 22°C. It is hypothesized that spinodal decomposition kinetics play a dominant role in determining the difference between skin and core morphologies for a given processing condition.

The authors are grateful to Courtaulds Corporate Technology (now part of the Acordis group) and the EPSRC for financial support, to John Robinson for sample sectioning, and to Dr. Nigel Briggs for help and advice. The X-ray experiments were performed on the ESRF beamline ID13.

REFERENCES

1. Coulsey, H. A.; Smith, S. B. Lenzinger Berichte 1996, 75, 51.
2. Schurz, J.; Lenz, J. Macromol Symp 1994, 83, 273.
3. Lenz, J.; Schurz, J.; Wrentschur, E. J Appl Polym Sci 1988, 35, 1987.
4. Briggs, N. Personal communication, 1998.
5. Ziabicki, A. Kolloid-Z 1961, 175, 14.
6. Ziabicki, A. Man-Made Fibers Science and Technology, Vol. 1; Wiley: New York/London/Sydney, 1967.
7. Smoulders, C. A.; Reuvers, A. J.; Broom, R. M.; Wienk, I. M. J Membr Sci 1992, 73, 259.
8. Fink, H. P.; Weigel, P.; Purz, H. J.; Bohn, A. Recent Research Developments in Polymer Science, 2nd ed.; Transworld Research Network: Kerala, India, 1998.
9. Müller, M.; Riekel, C.; Vuong, R.; Chanzy, H. Polymer 1999, 41, 2627.
10. Putnis, A. Introduction to Mineral Sciences; Cambridge Univ. Press: New York/London, 1992.
11. Mortimer, S. A.; Peguy, A. A. J Appl Polym Sci 1996, 60, 305.
12. Mortimer, S. A.; Peguy, A. A.; Ball, R. C. Cellul Chem Technol 1996, 30, 251.
13. Riekel, C.; Cedola, A.; Heidelbach, F.; Wagner, K. Macromolecules 1997, 30, 1033.
14. Huang, T. C.; Toraya, H.; Blanton, T. H.; Wu, Y. J Appl Crystallogr 1993, 26, 180.
15. Hammersley, A. FIT2D 2-D Detector Calibration/Correction; File Re-Formatting; 2-D Fitting; European Synchrotron Radiation Facility (ESRF), 1987–1997.
16. Balta-Calleja, F. J.; Vonk, C. J. X-Ray Scattering of Synthetic Polymers; Elsevier: Amsterdam/New York, 1989; Chapter 2.
17. Anton, H. Calculus with Analytic Geometry, 4th ed.; Wiley: New York, 1992.
18. Ruland, W. J Polym Sci Part C 1969, 28, 143.
19. Wang, W.; Ruland, W.; Cohen, Y. Acta Polym 1993, 44, 273.
20. Langford, J. I. J Appl Crystallogr 1978, 11, 10.
21. Peret, R.; Ruland,W. J Appl Crystallogr 1969, 2, 209.
22. Müller, M.; Czihak, C.; Vogl, G.; Fratzl, P.; Schober, H.; Riekel, C. Macromolecules 1998, 31, 3953.